mater.scichina.com link.springer.com

Published online 6 January 2023 | https://doi.org/10.1007/s40843-022-2295-8
Sci China Mater 2023, 66(5): 1861–1869

Silicon solar cell-enabled organic photoelectrochemical transistor optoelectronics

Yi-Tong Xu[1], Cheng Yuan[1], Bing-Yu Zhou[1], Zheng Li[1], Jin Hu[2], Peng Lin[2], Wei-Wei Zhao[1*], Hong-Yuan Chen[1] and Jing-Juan Xu[1*]

ABSTRACT Organic electrochemical transistors (OECTs) have been increasingly explored for innovative electronic devices. However, they inherently demand two power suppliers, which is unfavorable for the utilization of portable and wearable systems with strict energy requirements. Herein, by assembling a monocrystalline silicon solar cell into the OECT circuit with light as fuel, we demonstrated the possibility of a self-powered and light-modulated operation of organic photoelectrochemical transistor (OPECT) optoelectronics. Exemplified by poly(3,4-ethylenedioxythiophene):poly(styrenesulfonate) (PEDOT:PSS)-based depletion-mode and accumulation-mode OECTs, different light-addressable configurations were constructed, and the corresponding characteristics were systematically studied and compared. Different device behaviors with distinct characteristics could be achieved with the appropriate usage of light stimulation. Toward applications, optologics were designed with various parameters depending on the incident irradiance. Light-controlled OPECT unipolar inverters were further demonstrated and optimized with respect to the power source and resistance. This work features new OPECT optoelectronics combined with proper flexible substrates and solar cells for potential applications in portable and wearable devices.

Keywords: silicon solar cell, organic photoelectrochemical transistor, optoelectronics, light-addressable logic gate, light-controlled inverter

INTRODUCTION

The exploration of organic electrochemical transistors (OECTs) has recently seen tremendous growth in interdisciplinary fields, driven by the potential of this technique and the implementations that it may enable. Featuring good biocompatibility, high transconductance, and inherent amplification capability, various innovative bioelectronics [1–4], logic circuits [5–7], and neuromorphic devices [8–11] have been established upon OECTs. Essentially, operated upon the organic mixed ionic/electronic conductor (OMIEC), the volumetric ionic doping and de-doping of the polymeric channel interfacing the electrolyte could significantly modulate its bulk conductivity and hence amplify current responses under low voltages (within ±1 V) [12–14]. Their compatibility with flexible systems further makes OECTs promising in advanced wearables and other skin-interfaced applications, e.g., personal health monitoring and diagnostics [15–17]. However, such practical scenarios pose a challenge in terms of energy management. Generally, OECTs necessitate two instrumental power suppliers. The removal of one or even two of the power suppliers, with simultaneous energy harvesting from possible environmental sources, is significant for future biorelevant applications with stringent space and design restrictions.

To address this issue, efforts to pursue self-powered OECT operations have emerged. Sustainable solar, chemical, thermal, and mechanical energies are possible energy sources for such a purpose. For example, Ohayon *et al.* [18] presented an enzyme-coupled OECT that could collect chemical energy from samples to detect the glucose content. Yu *et al.* [19] designed a woven-structured triboelectric nanogenerator that could gather mechanical energy to operate OECT systems. Compared with piezoelectric materials or triboelectric nanogenerators, light is of interest for its noninvasive and contactless interplay with the harvester and the possibility of biorthogonal control with high spatiotemporal precision, thus attracting increasing attention in the community. Park *et al.* [20] introduced flexible photovoltaics that could harvest solar energy to power the OECT drain-source (d-s) circuit and transduce cardiac signals. Semiconductor gates have also been used by Winther-Jensen's and our group for logic gates [21] and organic photoelectrochemical transistor (OPECT) biosensing [22,23]. Despite these advances, the study in this field is still in its infancy, and remains to be explored.

In this work, we devised the concept of a monocrystalline silicon solar cell (MSSC)-enabled OPECT with self-powered capability and its representative optoelectronic applications toward light-addressable logic gates and light-controlled inverter. Specifically, the typical OMIEC of poly(3,4-ethylenedioxythiophene):poly(styrenesulfonate) (PEDOT:PSS) [12] and diethylenetriamine (DETA) de-doped PEDOT:PSS [24] were respectively used to construct the depletion-mode and accumulation-mode OECTs gated by a Ag/AgCl wire electrode. As illustrated in Fig. 1a$_1$–d$_1$, in the absence or presence of an MSSC, four possible combinations were constructed with depletion-mode OECTs. With the usage of an MSSC to power the d-s, gate-source (g-s), or both, we could obtain a distinct device performance in terms of the output and transfer characteristics and the corresponding transconductance evolution. Similarly, as

[1] State Key Laboratory of Analytical Chemistry for Life Science, School of Chemistry and Chemical Engineering, Nanjing University, Nanjing 210023, China
[2] Shenzhen Key Laboratory of Special Functional Materials & Guangdong Research Center for Interfacial Engineering of Functional Materials, College of Materials Science and Engineering, Shenzhen University, Shenzhen 518060, China
* Corresponding authors (emails: zww@nju.edu.cn (Zhao WW); xujj@nju.edu.cn (Xu JJ))

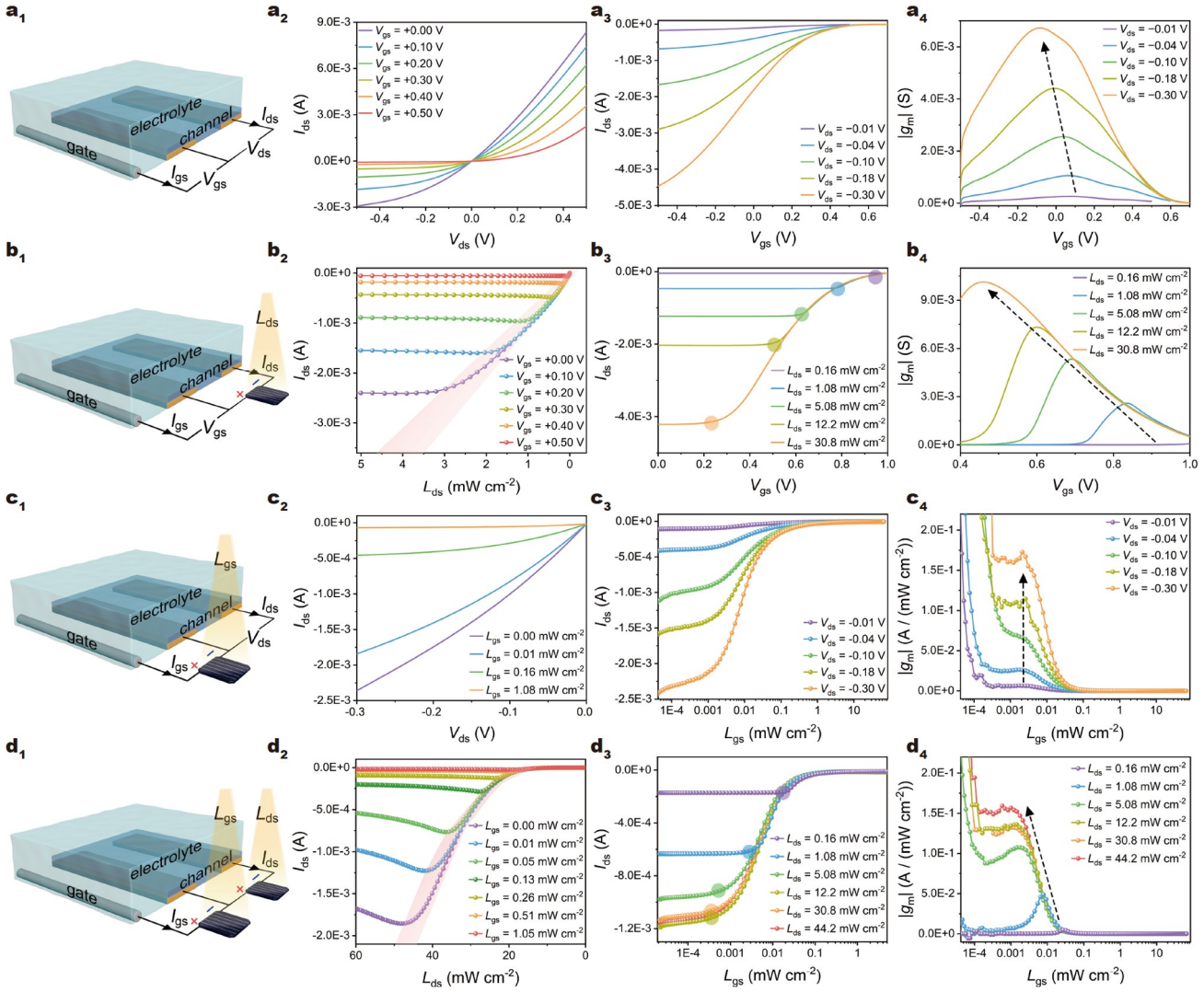

Figure 1 Schematic of the MSSC-enabled depletion-mode OECT and characteristics in the third quadrant. (a_1–d_1) represent OECT devices powered by two instrumental suppliers, MSSC for d-s, g-s, and both circuits, respectively. The arrows indicate the positive flow of the current measured by a galvanometer. (a_2–d_2), (a_3–d_3), and (a_4–d_4) represent the corresponding output, transfer characteristics, and transconductance evolution of the systems.

illustrated in Fig. 2a_1–d_1, the possible accumulation-mode counterparts were also constructed and characterized. For practical applications, novel light-addressable logic gates were successfully achieved as the appropriate implementation of the light could yield variant drain current (I_{ds}) responses. Moreover, a prototype light-controlled unipolar inverter capable of transferring a high (Hi) or low (Lo) input signal to the opposite output was developed. This work devotes to the fundamental study of light-fueled OECT devices and features the MSSC-enabled organic optoelectronics with promising self-powered and light-modulated applications, which, to our knowledge, has not been reported [25–27].

EXPERIMENTAL SECTION

Materials and apparatus

Phosphate-buffered saline (0.01 mol L^{-1}, 1 × PBS, pH 7.4) was purchased from Shanghai Yuanye Bio-Technology Co., Ltd. PEDOT:PSS (Clevios PH1000) was purchased from Heraeus. 3-Glycidyloxypropyl trimethoxysilane (GOPS) and DETA were obtained from Sigma-Aldrich. All the solutions were prepared with deionized water (Millipore, ≥18 MΩ cm). Current- and potential-related characterizations were conducted by utilizing a PEC/OPECT detector (Nandaguang, Nanjing, China).

Preparation of the channel part

The channel part of the depletion-mode OECT was fabricated according to our previous work [28] with a few modifications. Specifically, a glass substrate was orderly treated *via* ultrasonic cleaning in acetone, ethanol, and deionized water for 10 min and dried at 60°C. Then, the substrate was further treated with oxygen plasma. Afterward, the substrate was shielded with a template (channel length of 6.0 mm and width of 0.2 mm) and coated with 10 nm chromium and 100 nm gold *via* magnetron sputtering using the Kurt J. Lesker Company PRO Line PVD75 SP system (Kurt J. Lesker Company, USA). Next, the obtained substrate was further cleaned with oxygen plasma and spin-coated (500 r min^{-1} for 6 s and then 3500 r min^{-1} for 40 s) with the PEDOT:PSS solution (water:dimethyl sulfoxide = 95:5, *v*/*v*) to form a uniform film. Finally, the film was annealed at 150°C

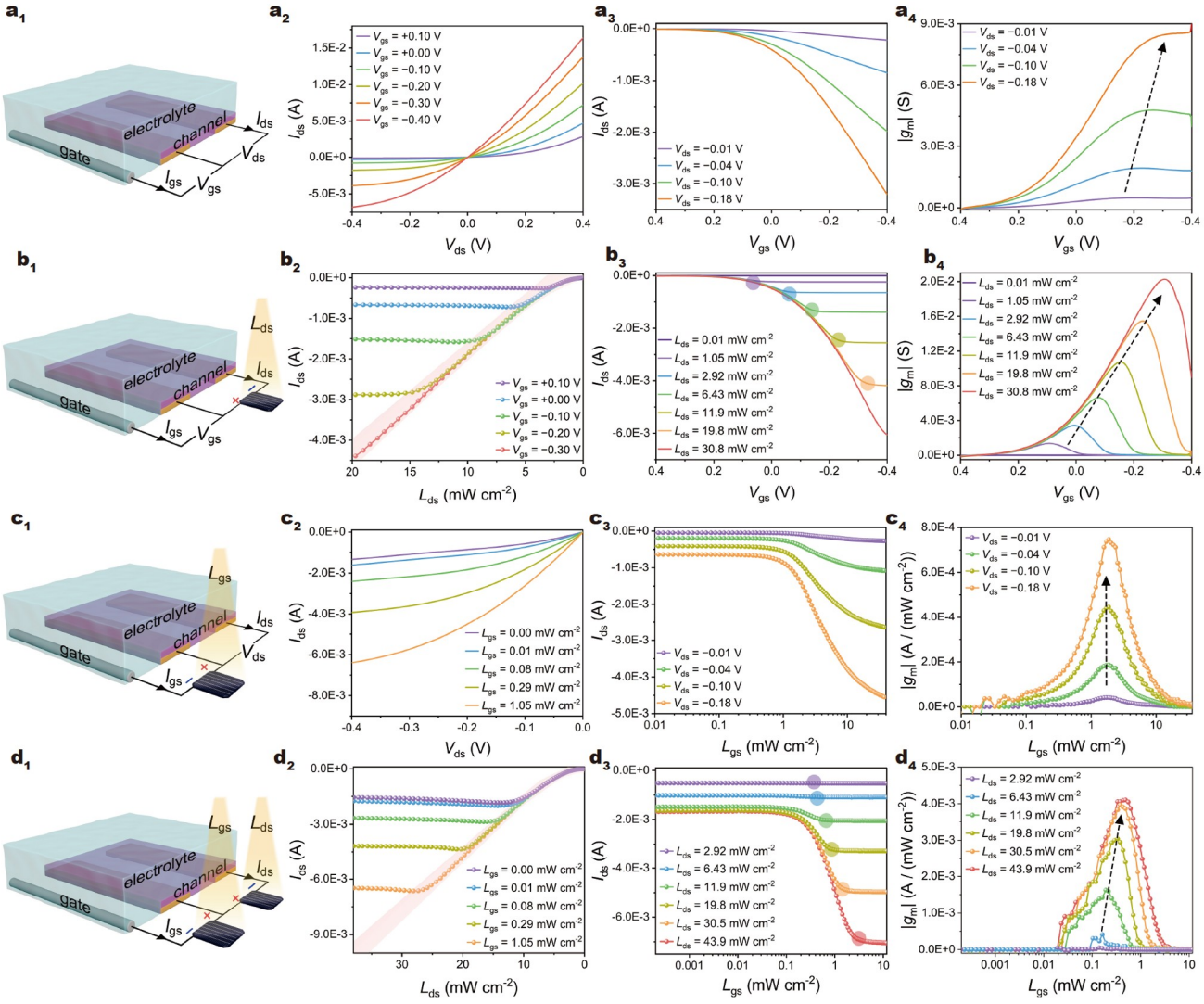

Figure 2 Schematic of the MSSC-enabled accumulation-mode OECT and characteristics in the third quadrant. (a_1–d_1) represent the OECT devices powered by two instrumental suppliers, MSSC for d-s, g-s, and both circuits, respectively. (a_2–d_2), (a_3–d_3), and (a_4–d_4) represent the corresponding output, transfer characteristics, and transconductance evolution of the systems, respectively.

for 1 h in an inert gas to stabilize the film. For the accumulation-mode OECT, the PEDOT:PSS solution was first mixed with 6 wt% ethylene glycol and 1 wt% GOPS. Then, the resulting solution was blended with 5% *v*/*v* DETA. The annealing process was set at 120°C for 20 min. When not in use, the devices were cleaned and kept dry in inert environments.

Experimental setup and data acquisition

During all the measurements, the channel parts were immersed in 1 × PBS. For output characteristics, the scanning voltages started from zero. For transfer characteristics, the scanning voltages were started from the on state for the depletion-mode OECT and from the off state for the accumulation-mode OECT. The time constants were extracted by fitting the exponential decay function: $I_{ds}(t) = I_{ds}(0) + a \times \exp(-t/\tau)$, where $I_{ds}(t)$ stands for the channel current at time t after the stimuli to the system, $I_{ds}(0)$ stands for the channel current upon stimuli, and τ stands for the time constant [29,30]. For all the light scanning operations, the transient current and open-circuit potential were recorded with simultaneous measurement of the transient irradiance.

RESULTS AND DISCUSSION

MSSC-enabled depletion-mode device

Fig. 1a_1 illustrates the diagram of a typical depletion-mode device powered by two instrumental suppliers. Principally, as shown in Fig. S1, the increasing anodic gate voltage (V_{gs}) can facilitate the diffusion of electrolyte cations into the polymeric channel. As a result, the hole density and conductance of the channel are decreased and *vice versa*. Fig. 1a_2 shows the corresponding output characteristics *versus* the scanning drain voltage (V_{ds}) under different V_{gs} stepped by 0.10 V. As V_{gs} increased from 0.00 to +0.50 V, although the absolute values of the I_{ds} decreased in the first and third quadrants, the characteristics exhibited essentially different behaviors. Specifically, it did not show saturation behavior in the first quadrant, whereas it tended to saturate as the V_{ds} became more negative [31]. The sub-

sequent characteristics in the two quadrants were thus respectively studied, with the ones of the third quadrant shown herein and those of the first quadrant in the Supplementary information (Fig. S2). As shown in Fig. 1a$_3$, at fixed V_{ds}, the absolute value of I_{ds} exhibited a gradual decrease with the increase in V_{gs}, while the transfer curves shifted to lower negative I_{ds} with the decrease in V_{ds} from −0.01 to −0.30 V. The corresponding evolution of transconductance ($|g_m| = \Delta I_{ds}/\Delta V_{gs}$) was further derived. As shown in Fig. 1a$_4$, as V_{ds} became more negative, the maximal transconductance exhibited a stepwise increase from 0.26, 1.05, 2.55, 4.41, to 6.73 mS, with the corresponding negative shift of V_{gs} from 0.077, 0.062, 0.040, −0.009, to −0.084 V, which could be attributed to the more negative V_{gs} needed to remove all cations from the drain electrode [32].

To construct the proposed MSSC-enabled device, as shown in Fig. S3, the photovoltaic properties of the used MSSC were characterized under different irradiances up to 100 mW cm^{-2} (AM1.5 sunlight conditions), with the maximal current intensity, open-circuit potential, and output power of 58.72 mA cm^{-2}, 0.578 V, and 6 mW, respectively, which was found to be capable of powering either the d-s or g-s circuit of the device. As illustrated in Fig. 1b$_1$, the d-s instrumental power supplier is substituted by the MSSC, and the irradiance is denoted as L_{ds}. As shown in Fig. 1b$_2$, the corresponding output characteristics were obtained by continuously increasing L_{ds} under different V_{gs}. Remarkably, the slopes of the I_{ds}-L_{ds} curves exhibited the same value in the saturation region, which could be attributed to the irradiance-dependent contact resistance in the d-s route. The curves tended to be very stable in the amplification region, which is beneficial to improving the device gain [33]. As shown in Fig. 1b$_3$, the corresponding transfer characteristics are recorded by scanning V_{gs} under different L_{ds}. Upon the light illumination, the device could be turned on and instantly enter a constant-current mode until a specific threshold V_{gs} (colored circles) started turning off the device from the on state. With the increase in L_{ds}, I_{ds} became more negative, and the threshold V_{gs} moved to a lower value, indicative of the smaller ΔV_{gs} needed to turn off the device. Significantly, such a behavior allows the light-controlled transition of the device performance and particularly the stable I_{ds} output within a low V_{gs} range for potential applications. As shown in Fig. 1b$_4$, the transconductances grew larger with the increase in L_{ds}, with the maximal transconductances moving to lower V_{gs}. At similar I_{ds} levels, greater transconductances were obtained as compared with those of the conventional OECT configuration. For example, as shown in Fig. 1a$_3$, a$_4$, the curves corresponded to V_{ds} = −0.30 V with I_{ds} of −4.46 mA, achieving a maximal transconductance of 6.73 mS, which was lower than that of 10.14 mS corresponding to the curves under 30.80 mW cm^{-2} with I_{ds} of −4.20 mA. The enhanced transconductances of the MSSC-enabled system were attributed to its higher effective V_{ds} than that of the conventional one.

Next, as illustrated in Fig. 1c$_1$, the g-s instrumental power supplier was substituted by the MSSC, and the irradiance was denoted as L_{gs}. Owing to the original on state of the PEDOT:PSS OECT, the positive pole of the MSSC was connected to the gate to shut off the system. As shown in Fig. 1c$_2$, the corresponding output characteristics were recorded by scanning V_{ds} under different L_{gs}. With the increase of L_{gs} from 0.00 to 1.08 mW cm^{-2}, I_{ds} exhibited a stepwise decrease until the off state. Such a behavior indicates its potential in-house application given the normal indoor irradiance within several mW cm^{-2} [34]. As shown in Fig. 1c$_3$, the corresponding transfer characteristics were recorded by the continuously increasing L_{gs} under different V_{ds}. Clearly, the transfer curves shifted to lower negative I_{ds} with the decrease in V_{ds} from −0.01 to −0.30 V, while the increased L_{gs} could inhibit the I_{ds} signals. L_{gs} of 1.08 mW cm^{-2} could turn off the device regardless of V_{ds}. The transconductances ($|g_m| = \Delta I_{ds}/\Delta$Irradiance) were also derived as a function of L_{gs}. As shown in Fig. 1c$_4$, the enhanced L_{gs} generally led to decreased transconductances. However, as V_{ds} changed from −0.01 to −0.30 V, five transconductance peaks of 6.19, 26.01, 66.13, 111.50, and 172.61 mA (mW cm^{-2})$^{-1}$ appeared at the same L_{gs} of 2.591 μW cm^{-2} on the curves.

As illustrated in Fig. 1d$_1$, the g-s and d-s instrumental power suppliers are then substituted by the MSSCs with individual light illumination. As shown in Fig. 1d$_2$, the corresponding output characteristics were measured by continuously increasing L_{ds} under different L_{gs}. In this case, the curves in the saturation region were again overlapped, but the curves exhibited concavities before entering the amplification region. As compared with the ca. 4 mW cm^{-2} of L_{ds} at V_{gs} of 0 V in Fig. 1b$_2$, ca. 40 mW cm^{-2} of L_{ds} was needed to make it leave the saturation region, which could be attributed to the enhanced resistance of the MSSC within the circuit. Remarkably, the output I_{ds} could still be effectively inhibited by a low L_{gs}, e.g., 0.51 mW cm^{-2}. As shown in Fig. 1d$_3$, the transfer characteristics are obtained by continuously increasing L_{gs} under different L_{ds}. Upon the application of L_{ds}, the device could be turned on, and I_{ds} increased up to ca. −1.13 mA with the enhanced L_{ds} up to 12.2 mW cm^{-2}. Moreover, with the increase in L_{ds}, the threshold L_{gs} (colored circles) also moved to a lower value. Compared with 1.08 mW cm^{-2} of the case in Fig. 1c$_3$, a smaller L_{gs} of 0.1 mW cm^{-2} was needed to turn off the device. The corresponding transconductances were derived, as shown in Fig. 1d$_4$. As compared with those in Fig. 1c$_4$, the peak transconductances and the corresponding L_{gs} were adjustable depending upon the variant L_{ds}.

MSSC-enabled accumulation-mode device

Compared with the depletion-mode device, the accumulation-mode type possesses different behaviors, e.g., a natural off state with smaller I_{ds} at the zero gate bias. As shown in Fig. S4, the oxidized DETA [24] was utilized to de-dope the PEDOT:PSS polymer and construct the accumulation-mode OECT. Fig. 2a$_1$ illustrates the diagram of such a device powered by two instrumental suppliers. Fig. 2a$_2$ shows the corresponding output characteristics by scanning V_{ds} under different V_{gs} stepping from +0.10 to −0.40 V. Similar to those in the depletion-mode type, the characteristics in the two quadrants were also studied, with the ones of the third quadrant shown herein and those of the first quadrant in the Supplementary information (Fig. S5). As shown in Fig. 2a$_3$, at a fixed V_{ds}, the absolute value of I_{ds} exhibited a gradual increase with the decrease in V_{gs}, and the transfer curves shifted to a lower negative I_{ds} with the decrease in V_{ds} from −0.01 to −0.18 V. As shown in Fig. 2a$_4$, as V_{ds} became more negative, the maximal transconductance exhibited a stepwise increase from 0.49, 1.94, 4.79, to 8.52 mS, with the corresponding negative shift of V_{gs} from −0.206, −0.232, −0.264, to −0.336 V.

Then, as illustrated in Fig. 2b$_1$, the d-s instrumental power supplier was substituted by the MSSC. As shown in Fig. 2b$_2$, the

corresponding output characteristics were obtained by continuously increasing L_{ds} under different V_{gs}. The slopes of the I_{ds}-L_{ds} curves exhibited the same value in the saturation region, and the curves tended to be very stable in the amplification region. As shown in Fig. 2b$_3$, the corresponding transfer characteristics were recorded by scanning V_{gs} under different L_{ds}. Upon the light illumination, I_{ds} was kept in the off state and then increased to lower negative with V_{gs} decreasing until a specific threshold V_{gs}' (colored circles) that could keep the device on. With the increase in L_{ds}, the on state I_{ds} became more negative, and the threshold V_{gs}' moved to a negative value, indicative of the smaller ΔV_{gs} needed to turn on the device. As shown in Fig. 2b$_4$, the transconductances grew larger with the increase in L_{ds}, with the maximal transconductances moved to a lower V_{gs}. Moreover, at similar I_{ds} levels, greater transconductances were obtained as compared with those in Fig. 2a$_4$. For example, as shown in Fig. 2a$_3$, a$_4$, the curves corresponded to V_{ds} = −0.18 V with I_{ds} of −3.19 mA, achieving a maximal transconductance of 8.52 mS, which was lower than that of 10.74 mS corresponding to the curves under 11.9 mW cm^{-2} with I_{ds} of −2.56 mA.

Next, as illustrated in Fig. 2c$_1$, the g-s instrumental power supplier was substituted by the MSSC. Due to the original off state of this accumulation-mode OECT, the negative pole of the MSSC was connected to the gate to turn on the system. As shown in Fig. 2c$_2$, the corresponding output characteristics were recorded by scanning V_{ds} under different L_{gs}. With the increase in L_{gs} from 0.00 to 1.05 mW cm^{-2}, the absolute I_{ds} exhibited a stepwise increase. As shown in Fig. 2c$_3$, the corresponding transfer characteristics were recorded by continuously increasing L_{gs} under different V_{ds}. Clearly, the transfer curves shifted to lower negative I_{ds} with the decrease in V_{ds} from −0.01 to −0.18 V, while the increased L_{gs} could further boost the I_{ds} signals. In particular, L_{gs} of 1.08 mW cm^{-2} could start to turn on the device regardless of V_{ds}. The corresponding transconductances were also derived. As shown in Fig. 2c$_4$, as V_{ds} changed from −0.01 to −0.18 V, four transconductance peaks of 0.04, 0.19, 0.45, and 0.75 mA (mW cm^{-2})$^{-1}$ appeared at the same L_{gs} of 1.879 mW cm^{-2} on the curves.

As illustrated in Fig. 2d$_1$, the g-s and d-s instrumental power suppliers were then substituted by the MSSCs with individual light illumination. As shown in Fig. 2d$_2$, the corresponding output characteristics were measured by continuously increasing L_{ds} under different L_{gs}. In this case, the curves in the saturation region were again overlapped, and the curves tended to be very stable in the amplification region. As compared with ca. 5.5 mW cm^{-2} of L_{ds} at V_{gs} of 0 V in Fig. 2b$_2$, ca. 11.0 mW cm^{-2} of L_{ds} was needed to make it leave the saturation region, which could be attributed to the enhanced resistance of the MSSC within the circuit. Remarkably, the output I_{ds} could still be effectively enhanced by a low L_{gs}, e.g., 1.05 mW cm^{-2}. As shown in Fig. 2d$_3$, the transfer characteristics were obtained by continuously increasing L_{gs} under different L_{ds}. Upon the application of varied L_{ds}, the device started to work with the I_{ds} stationed at different off states. With L_{gs} increasing, the I_{ds} increased to a lower negative and then became constant after a specific threshold L_{gs}' (colored circles), and the corresponding threshold L_{gs}' also moved to a higher value. Compared with more than tens of mW cm^{-2} of the case in Fig. 2c$_3$, a smaller L_{gs} within 5 mW cm^{-2} was needed to turn on I_{ds}. The corresponding transconductances were derived, as shown in Fig. 2d$_4$. As compared with those in Fig. 2c$_4$, the peak transconductances were several times larger and the corresponding L_{gs} were adjustable in a lower irradiance range (within 1 mW cm^{-2}) dependent upon the variant L_{ds}.

Light-addressable optologics

Light-addressable modules utilizing light to yield specific signals have been long pursued and applied in the fields of sensing [35], diagnostics [36], and bio-emulation [37,38], and logic circuits executing a processing or controlling function have been widely used in various scientific and industrial scenarios [39–41]. In this study, our devices were tested for innovative light-addressable optologics. As illustrated in Fig. 3a$_1$–a$_4$, upon different combinations of light irradiation, four combinations of input signals were denoted as (0, 0), (1, 0), (0, 1), and (1, 1), respectively. Using a depletion-mode OECT, Fig. 3b shows a representative light-addressable combinatorial logic consisting of an AND gate and a NOT gate, which was established upon the programmed application of L_{ds} and L_{gs}, as illustrated in Fig. 3b$_1$, b$_2$, respectively. As shown in the results, within 0–5 s, upon the "off" state of L_{ds} and L_{gs}, the system kept its status of (0, 0), which was changed to (1, 0) upon the "on" state of L_{ds}. Within 5–45 s, repeated "off/on" of L_{ds} would lead to the switch between (0, 0) and (1, 0). From 45–75 s, the "on" state of both L_{ds} and L_{gs} would alter the system to (1, 1), and the output intensities could be controlled by different input irradiances of L_{ds} and L_{gs}. Fig. 3c$_1$–c$_5$ show the corresponding output behaviors at L_{ds} of 0.16, 1.08, 5.08, 12.2, 30.80 mW cm^{-2}, respectively, with different L_{gs} of 0.01 (purple), 0.10 (blue), 0.30 (green), 1.05 (orange) mW cm^{-2}. Specifically, following the onset of (1, 0), the I_{ds} increased promptly from 0 to specific intensity, which grew gradually with enhanced irradiance of L_{ds}. Meanwhile, following the onset of (0, 0), the I_{ds} decreased promptly to 0. Such a behavior indicates the light-controllable fast response of the system. Note that the spikes appeared due to the faster rate of electron transportation in the wire than the hole extraction/transportation in the channel [29]. With the increased irradiance of L_{ds}, more prominent spiked I_{ds} was observed, which was due to the larger accelerated rate of electron transportation and made this device hold great promise in futuristic biomimicking of photoadaptation [42–44]. Upon the further on/off application of L_{gs} of variant irradiances, the I_{ds} would respond to different levels with different speeds and on/off ratios. Overall, in such a configuration, (1, 0) was denoted as the on state of I_{ds}, whereas (1, 1) was denoted as the off state of I_{ds}. As shown in Fig. 3d–f, with the increased irradiances of both L_{ds} and L_{gs}, the time constant for switching I_{ds} from the off to the on state (τ_{on}) was increased from 0.071 to 1.041 s, whereas the time constant for switching I_{ds} from the on state to the off state (τ_{off}) was reduced from 1.245 to 0.031 s, with the corresponding on/off ratios increasing from 1.002 to 50.849. τ_{off} became smaller and τ_{on} became larger with the increase in L_{gs} at a certain L_{ds}, which could be attributed to the transportation of more cations into the channel.

Meanwhile, using an accumulation-mode OECT, Fig. 3g shows a representative light-addressable AND gate, which was established upon the programmed application of L_{ds} and L_{gs}, as illustrated in Fig. 3g$_1$, g$_2$, respectively. Fig. 3h$_1$–h$_5$ show the corresponding output behaviors at L_{ds} of 0.16, 1.08, 5.08, 12.20, and 30.8 mW cm^{-2}, respectively, with different L_{gs} of 0.01 (purple), 0.29 (blue), 1.05 (green), and 2.92 (orange) mW cm^{-2}. Specifically, the switch between (1, 0) and (0, 0) also led to the

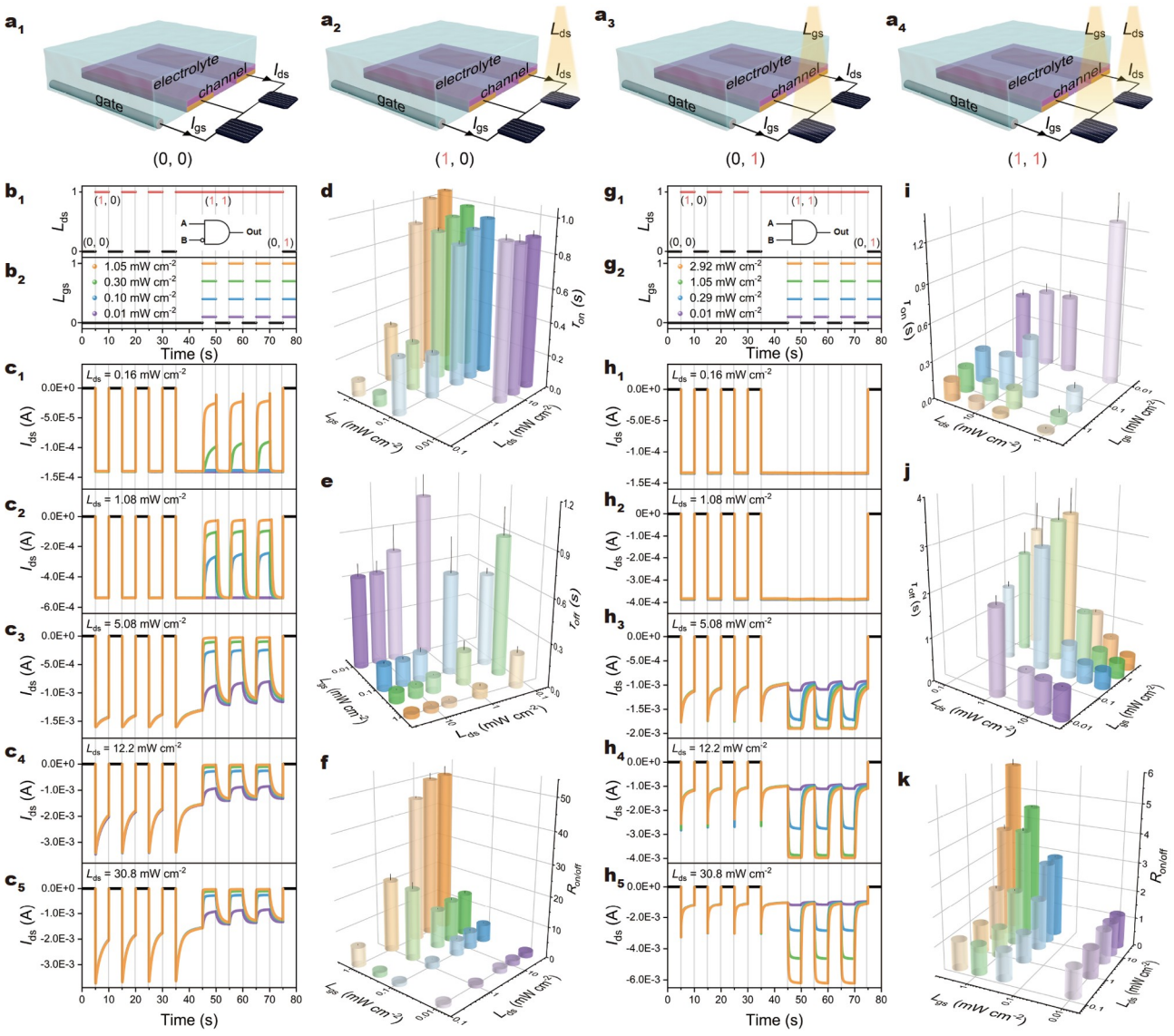

Figure 3 Totally MSSC-enabled OECT for light-addressable logic gates. (a_1–a_4) Setups and the corresponding input truth values of four combinations, denoted as (0, 0), (1, 0), (0, 1), and (1, 1), respectively. Programmed light inputs (b_1, b_2), output I_{ds} responses (c_1–c_5), the τ_{on}, τ_{off}, and on/off ratios (d–f) of the depletion-mode OECT. Programmed light inputs (g_1, g_2), output I_{ds} responses (h_1–h_5), τ_{on}, τ_{off}, and on/off ratios (i–k) of the accumulation-mode OECT. Insets in (b_1) and (g_1) show the corresponding logic symbols.

prompt rise and decrease of I_{ds}, but the spiked I_{ds} of high irradiances of L_{ds} exhibited a faster decay. Upon further combinatorial usage of variants L_{ds} and L_{gs}, I_{ds} would also exhibit different behaviors. At lower L_{ds} (0.16 and 1.08 mW cm^{-2}), the application of L_{gs} could not affect the device, whereas I_{ds} increased with the increased irradiance of L_{gs} at higher L_{ds} (5.08, 12.2, and 30.8 mW cm^{-2}). Overall, in such a configuration, (1, 0) was denoted as the off state of I_{ds}, whereas (1, 1) was denoted as the on state of I_{ds}. As shown in Fig. 3i–k, τ_{on} was reduced with increasing L_{gs} (above 0.29 mW cm^{-2}) and decreasing L_{ds}, τ_{off} was reduced with increasing L_{ds} (within 12.2 mW cm^{-2}) and decreasing in L_{gs} (above 0.29 mW cm^{-2}), and the on/off ratios increased with increased light irradiance.

Light-controlled unipolar inverter

Inverters are basic components for constructing circuits with NOT logicality. Bridging the biological world and data processing, OECT-based inverters have been exploited for sensing ionic [45] and physiological signals [46], which, nevertheless, have not been achieved upon light stimulation. To make OECT-based inverters capable of communication with a photonic medium, we demonstrated the first light-controlled unipolar OECT inverter by integrating MSSCs into the g-s circuit of the OECT. As illustrated in Fig. 4a, the proposed inverter was composed of lithium battery power suppliers ($+V_{dd}$ and $-V_{dd}$), three adjustable resistances (R_1 = 1.5R_2 = 3R_3), and an MSSC-enabled depletion-mode OECT in parallel with R_3, with light signals as the input (L_{in}) and voltage signals as the output (V_{out}). Fig. 4b–d show the corresponding transfer characteristics with different R_1 values under V_{dd} = 1.2, 1.5, and 2.4 V, respectively. When L_{in} was smaller than 0.1 mW cm^{-2}, the OECT channel was in the low-resistance state (R_{ch} << R_3), and the current in the

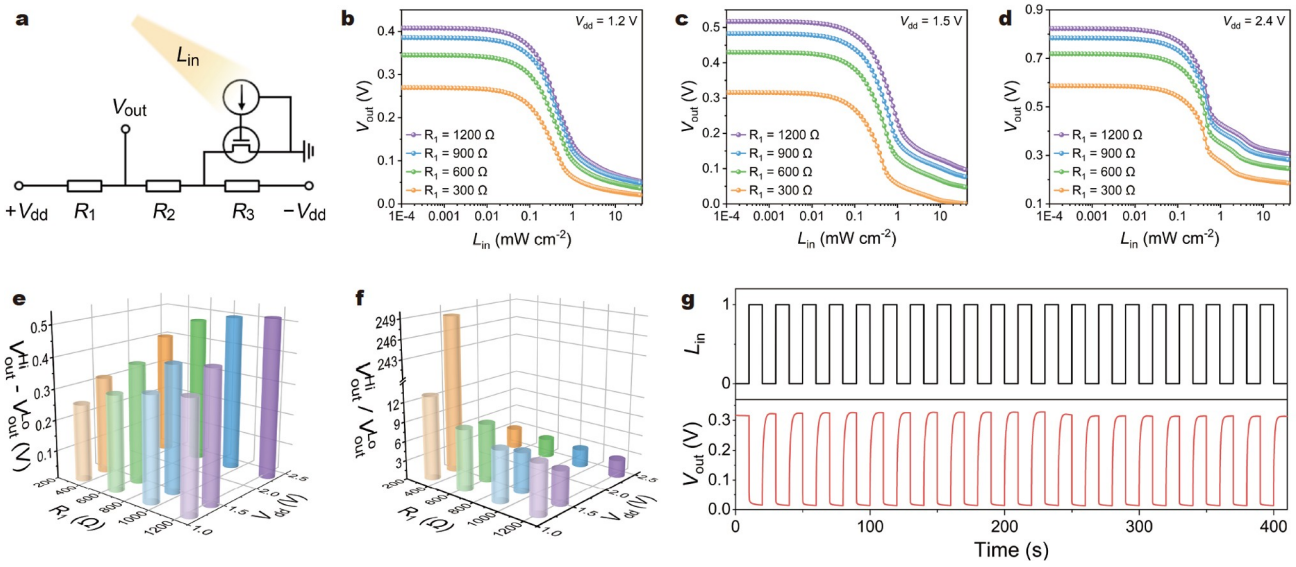

Figure 4 Properties of the light-controlled unipolar inverter. (a) Schematic of the inverter layout. (b–d) Transfer characteristics with different R_1 under V_{dd} of 1.2, 1.5, and 2.4 V, respectively. (e, f) Dependences of V_{out} differences and ratios on V_{dd} and R_1. (g) Output characteristics of the inverter under V_{dd}, R_1, and L_{in} of 1.5 V, 300 Ω, and 43.9 mW cm^{-2}, respectively.

system mainly flowed from $+V_{dd}$, R_1, R_2, to the OECT channel part, then to the ground, resulting in a higher potential drop between V_{out} contact and the ground, and thus higher V_{out} (V_{out}^{Hi}). With L_{in} increasing from 0.01 to 10 mW cm^{-2}, V_{out} dramatically declined. When L_{in} was stronger than 10 mW cm^{-2}, the OECT channel was in the high-resistance state (R_{ch} >> R_3), and the current in the system mainly flowed from $+V_{dd}$, R_1, R_2, and R_3, then to $-V_{dd}$, resulting in a much smaller potential drop between the V_{out} contact and the ground and thus lower V_{out} (V_{out}^{Lo}). Fig. 4e, f summarize the dependences of V_{out} differences ($V_{out}^{Hi} - V_{out}^{Lo}$) and the ratios ($V_{out}^{Hi} / V_{out}^{Lo}$) of the V_{dd} and R_1 values. With the increases in V_{dd} and R_1, the V_{out} differences were stepwise enhanced from 0.249 to 0.516 V. With the decreases in V_{dd} and R_1, the V_{out} ratios were generally elevated, and a peak value of 248.82 was obtained under V_{dd} of 1.5 V and R_1 of 300 Ω, which was chosen to further investigate the output characteristics of the system. As shown in Fig. 4g, with repeated L_{in} on/off cycles up to 20 times and 400 s, V_{out} was periodically switched between 0.326 and 0.014 V with negligible degradation, suggesting the good reversibility of the system.

CONCLUSION

In conclusion, MSSC-enabled OPECT optoelectronics were devised with self-powered and light-modulated capabilities, which were further implemented toward novel light-addressable optologics and light-controlled unipolar inverters. The characteristics of the MSSC-enabled device in the first and third quadrants were systematically studied, and the results reveal the overall superior modulation abilities in the third quadrant. Remarkably, the MSSC in the d-s circuit could significantly enhance the amplification and transconductance compared with the conventional OECT, while the MSSC in the g-s circuit could effectively regulate output signals under indoor irradiance. Based on the totally MSSC-enabled device, the signal-on and signal-off types of light-addressable logic circuits were constructed with a potential utility toward optoelectronics and biomimicry. Furthermore, a light-controlled unipolar inverter was realized and optimized, demonstrating good reversibility against incident illumination. The proposed MSSC-enabled OPECT optoelectronics not only hold the promise of autonomous optoelectronic devices for data processing and signal emulation, but also could be helpful in the future energy management of portable and wearable devices, given its proper adaption to flexible and soft systems.

Received 20 August 2022; accepted 21 October 2022; published online 6 January 2023

1 Koklu A, Wustoni S, Guo K, *et al.* Convection driven ultrarapid protein detection *via* nanobody-functionalized organic electrochemical transistors. Adv Mater, 2022, 34: 2202972
2 Li W, Jin J, Xiong T, *et al.* Fast-scanning potential-gated organic electrochemical transistors for highly sensitive sensing of dopamine in living rat brain. Angew Chem Int Ed, 2022, 61: e202204134
3 Strakosas X, Donahue MJ, Hama A, *et al.* Biostack: Nontoxic metabolite detection from live tissue. Adv Sci, 2022, 9: 2101711
4 Liu H, Yang A, Song J, *et al.* Ultrafast, sensitive, and portable detection of COVID-19 IgG using flexible organic electrochemical transistors. Sci Adv, 2021, 7: eabg8387
5 Nguyen-Dang T, Chae S, Chatsirisupachai J, *et al.* Dual-mode organic electrochemical transistors based on self-doped conjugated polyelectrolytes for reconfigurable electronics. Adv Mater, 2022, 34: 2200274
6 Granelli R, Alessandri I, Gkoupidenis P, *et al.* High-performance bioelectronic circuits integrated on biodegradable and compostable substrates with fully printed mask-less organic electrochemical transistors. Small, 2022, 18: 2108077
7 Makhinia A, Hübscher K, Beni V, *et al.* High performance organic electrochemical transistors and logic circuits manufactured *via* a combination of screen and aerosol jet printing techniques. Adv Mater Technologies, 2022, 7: 2200153
8 Harikesh PC, Yang CY, Tu D, *et al.* Organic electrochemical neurons and synapses with ion mediated spiking. Nat Commun, 2022, 13: 901
9 Zhang Y, Ye G, van der Pol TPA, *et al.* High-performance organic electrochemical transistors and neuromorphic devices comprising naphthalenediimide-dialkoxybithiazole copolymers bearing glycol ether pendant groups. Adv Funct Mater, 2022, 32: 2201593
10 Yamamoto S, Polyravas AG, Han S, *et al.* Correlation between transient

response and neuromorphic behavior in organic electrochemical transistors. Adv Elect Mater, 2022, 8: 2101186
11 Janzakova K, Ghazal M, Kumar A, *et al.* Dendritic organic electrochemical transistors grown by electropolymerization for 3D neuromorphic engineering. Adv Sci, 2021, 8: 2102973
12 Khodagholy D, Rivnay J, Sessolo M, *et al.* High transconductance organic electrochemical transistors. Nat Commun, 2013, 4: 2133
13 Lee SK, Cho YW, Lee JS, *et al.* Nanofiber channel organic electrochemical transistors for low-power neuromorphic computing and wide-bandwidth sensing platforms. Adv Sci, 2021, 8: 2001544
14 Bianchi M, De Salvo A, Asplund M, *et al.* Poly(3,4-ethylenedioxythiophene)-based neural interfaces for recording and stimulation: Fundamental aspects and *in vivo* applications. Adv Sci, 2022, 9: 2104701
15 Wang J, Lee S, Yokota T, *et al.* Gas-permeable organic electrochemical transistor embedded with a porous solid-state polymer electrolyte as an on-skin active electrode for electrophysiological signal acquisition. Adv Funct Mater, 2022, 32: 2200458
16 Dai Y, Dai S, Li N, *et al.* Stretchable redox-active semiconducting polymers for high-performance organic electrochemical transistors. Adv Mater, 2022, 34: 2201178
17 Chen J, Huang W, Zheng D, *et al.* Highly stretchable organic electrochemical transistors with strain-resistant performance. Nat Mater, 2022, 21: 564–571
18 Ohayon D, Nikiforidis G, Savva A, *et al.* Biofuel powered glucose detection in bodily fluids with an n-type conjugated polymer. Nat Mater, 2020, 19: 456–463
19 Yu J, Qin S, Zhang H, *et al.* Fiber-shaped triboiontronic electrochemical transistor. Research, 2021, 2021: 1–10
20 Park S, Heo SW, Lee W, *et al.* Self-powered ultra-flexible electronics *via* nano-grating-patterned organic photovoltaics. Nature, 2018, 561: 516–521
21 Kolodziejczyk B, Ng CH, Strakosas X, *et al.* Light sensors and optologic gates based on organic electrochemical transistors. Mater Horiz, 2018, 5: 93–98
22 Hu J, Lu MJ, Chen FZ, *et al.* Multifunctional hydrogel hybrid-gated organic photoelectrochemical transistor for biosensing. Adv Funct Mater, 2022, 32: 2109046
23 Xu YT, Li Z, Yuan C, *et al.* Bipolar modulation of the ionic circuit for generic organic photoelectrochemical transistor logic and sensor. Adv Opt Mater, 2022, 10: 2102687
24 Keene ST, Pol TPA, Zakhidov D, *et al.* Enhancement-mode PEDOT:PSS organic electrochemical transistors using molecular de-doping. Adv Mater, 2020, 32: 2000270
25 Rivnay J, Inal S, Salleo A, *et al.* Organic electrochemical transistors. Nat Rev Mater, 2018, 3: 17086
26 Wang N, Yang A, Fu Y, *et al.* Functionalized organic thin film transistors for biosensing. Acc Chem Res, 2019, 52: 277–287
27 Rashid RB, Ji X, Rivnay J. Organic electrochemical transistors in bioelectronic circuits. Biosens Bioelectron, 2021, 190: 113461
28 Lu MJ, Chen FZ, Hu J, *et al.* Regulating light-sensitive gate of organic photoelectrochemical transistor toward sensitive biodetection at zero gate bias. Small Struct, 2021, 2: 2100087
29 Bernards D, Malliaras G. Steady-state and transient behavior of organic electrochemical transistors. Adv Funct Mater, 2007, 17: 3538–3544
30 Giovannitti A, Sbircea DT, Inal S, *et al.* Controlling the mode of operation of organic transistors through side-chain engineering. Proc Natl Acad Sci USA, 2016, 113: 12017–12022
31 Nilsson D, Robinson N, Berggren M, *et al.* Electrochemical logic circuits. Adv Mater, 2005, 17: 353–358
32 Paudel PR, Kaphle V, Dahal D, *et al.* Tuning the transconductance of organic electrochemical transistors. Adv Funct Mater, 2021, 31: 2004939
33 Sporea RA, Trainor MJ, Young ND, *et al.* Source-gated transistors for order-of-magnitude performance improvements in thin-film digital circuits. Sci Rep, 2014, 4: 4295
34 Reinders AHME, van Sark WGJHM. 1.34-Product-integrated photovoltaics. In: Sayigh A. Comprehensive Renewable Energy. Cambridge: Elsevier, 2012, 1: 709
35 Zhao CQ, Ding SN. Perspective on signal amplification strategies and sensing protocols in photoelectrochemical immunoassay. Coord Chem Rev, 2019, 391: 1–14
36 Crespi S, Simeth NA, König B. Heteroaryl azo dyes as molecular photoswitches. Nat Rev Chem, 2019, 3: 133–146
37 Han B, Zhang YL, Zhu L, *et al.* Plasmonic-assisted graphene oxide artificial muscles. Adv Mater, 2018, : 1806386
38 Song S, Kim M, Yoo G, *et al.* Solution-processed oxide semiconductor-based artificial optoelectronic synapse array for spatiotemporal synaptic integration. J Alloys Compd, 2021, 857: 158027
39 Zhou F, Liu Y, Shen X, *et al.* Low-voltage, optoelectronic $CH_3NH_3PbI_{3-x}Cl_x$ memory with integrated sensing and logic operations. Adv Funct Mater, 2018, 28: 1800080
40 Shan Z, Hu X, Wang X, *et al.* Phonon-assisted electro-optical switches and logic gates based on semiconductor nanostructures. Adv Mater, 2019, 31: 1901263
41 Chen J, Ouyang W, Yang W, *et al.* Recent progress of heterojunction ultraviolet photodetectors: Materials, integrations, and applications. Adv Funct Mater, 2020, 30: 1909909
42 Shen H, He Z, Jin W, *et al.* Mimicking sensory adaptation with dielectric engineered organic transistors. Adv Mater, 2019, 31: 1905018
43 Xie D, Wei L, Xie M, *et al.* Photoelectric visual adaptation based on 0D-$CsPbBr_3$-quantum-dots/2D-MoS_2 mixed-dimensional heterojunction transistor. Adv Funct Mater, 2021, 31: 2010655
44 He Z, Shen H, Ye D, *et al.* An organic transistor with light intensity-dependent active photoadaptation. Nat Electron, 2021, 4: 522–529
45 Romele P, Gkoupidenis P, Koutsouras DA, *et al.* Multiscale real time and high sensitivity ion detection with complementary organic electrochemical transistors amplifier. Nat Commun, 2020, 11: 3743
46 Rashid RB, Du W, Griggs S, *et al.* Ambipolar inverters based on cofacial vertical organic electrochemical transistor pairs for biosignal amplification. Sci Adv, 2021, 7: eabh1055

Acknowledgements This work was supported by the National Natural Science Foundation of China (22034003, 21974059, and 22174063), the Excellent Research Program of Nanjing University (ZYJH004), and the State Key Laboratory of Analytical Chemistry for Life Science (5431ZZXM2203).

Author contributions Xu YT designed and performed the testing; Yuan C and Zhou BY fabricated the devices; Li Z visualized the data; Hu J examined the methodology; Lin P reviewed the manuscript; Zhao WW conceived the concept and supervised the experiments; Chen HY and Xu JJ administrated the project and supervised the experiments. All the authors contributed to the general discussion.

Conflict of interest The authors declare that they have no conflict of interest.

Supplementary information Experiment details and supporting data are available in the online version of the paper.

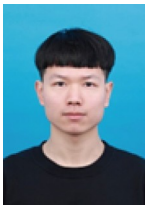

Yi-Tong Xu obtained his BSc degree from Harbin Institute of Technology in 2018. He is currently pursuing his PhD degree with Profs Wei-Wei Zhao, Jing-Juan Xu and Hong-Yuan Chen at Nanjing University (NJU). His research focuses on developing new electrochemical methods for biosensing and functional electronic devices.

Wei-Wei Zhao was educated at Nanjing University of Aeronautics and Astronautics and received his BSc and ME degrees in 2005 and 2008, respectively. Then he moved to NJU and received his PhD degree in 2012. Currently, he works at NJU as an associate professor, and his research focuses on bio-detection and advanced electrochemical techniques.

Jing-Juan Xu graduated from Wuhan University in 1990 and earned her MSc and PhD degrees from NJU in 1997 and 2000. Currently, she is a full professor at the Department of Chemistry, NJU. Her research interest focuses on the development of various optical/electrochemical probes and devices based on advanced functional nanomaterials with enhanced performances for biological analysis.

硅太阳能电池供能的有机电化学晶体管光电子器件

徐一童[1], 袁骋[1], 周冰煜[1], 李政[1], 胡进[2], 林鹏[2], 赵伟伟[1*], 陈洪渊[1], 徐静娟[1*]

摘要 越来越多的研究将有机电化学晶体管(OECT)用于新颖的电学设备, 然而这些设备天然需要两个仪器电源, 不利于将其应用于对能源供应有严格要求的便携和可穿戴体系. 本文通过将单晶硅太阳能电池组装到OECT的回路中并以光作为燃料, 构建了自供能和光调控功能的有机光电化学晶体管(OPECT)光电子器件. 以基于聚(3,4-乙烯二氧噻吩)-聚(苯乙烯磺酸酯) (PEDOT:PSS)的耗尽型和增强型OECT为例, 我们设计了不同的光寻址结构并系统地研究和比较了相应的特性. 通过合适的光调制, 我们实现了不同的器件行为, 且这些器件表现出优异的性能. 在应用层面, 我们设计了光逻辑电路, 其不同的特性可以通过相应的辐照度来调控; 此外, 我们展示了光控的OECT单极逆变器, 并根据系统的能源供应和阻抗进行了优化. 本工作代表着新型的OPECT光电子器件, 合理地将其与柔性基底和太阳能电池组装有望应用于便携和可穿戴器件领域.